https://doi.org/10.5194/egusphere-2025-4396
Preprint. Discussion started: 23 September 2025

Predicting the amplitude and runup of the water waves induced by rotational cliff collapse, considering fragmentation

Hasnain Gardezi[a*], Talha Khan[c], Xingyue Li [a,b*], Taimur Mazhar Sheikh[a], Yu Huang [a,b], Zhiyi Chen [a]

[a] Department of Geotechnical Engineering, College of Civil Engineering, Tongji University, Shanghai 200092, China

[b] State Key Laboratory of Disaster Reduction in Civil Engineering, Tongji University, Shanghai 200092, China

[c] School of Aerospace Engineering and Applied Mechanics, Tongji University, Shanghai 200092, China

*Corresponding authors: hasnain_haider@tongji.edu.cn (Hasnain Gardezi), xingyueli@tongji.edu.cn (X.Y.Li)

Abstract:

Cliff collapse-induced water waves in small lakes and reservoirs retain their energy due to short travel distance, and may cause significant damage to offshore infrastructure. Previously, scientists have analyzed the waves induced by granular/block sliding down the slope and hitting a water body, but none have studied the water waves induced by rotational cliff collapse, fragmenting upon impact with the water surface. So, in this study, we have experimentally and numerically analyzed the rotational cliff collapse and energy transfer mechanism, determined the amplitude and runup of the induced waves, and developed machine learning-based prediction models. Moreover, the effect of the fragmentation of the cliff upon impact on the induced wave has also been investigated. The results indicate that as the water depth decreases, the impact Froude number and relative wave amplitude increase, wave velocity decreases, and the splash becomes more elongated. A comparison between the wave induced by fragmented cliff collapse and an equivalent amount of granular mass sliding from a 30° slope indicates that the amplitude of the waves induced by granular mass is 42%, 35%, and 28% less than that of fragmented cliff collapse. The wave amplitude induced by fragmented cliff collapse indicates that the rotational motion of the cliff imparts a more sudden and concentrated impact that allows an efficient energy transfer to water, resulting in higher wave amplitudes. The results for the prediction model indicate that the amplitude and runup model performed well both in the training and testing stages, with higher R^2

https://doi.org/10.5194/egusphere-2025-4396
Preprint. Discussion started: 23 September 2025

values. The developed model was validated by comparing the results with established statistical indices and by performing sensitivity and parametric analysis, highlighting that wave amplitude is greatly influenced by impact velocity, cliff height, and the number of fragments, contributing approximately 90% to the wave amplitude. In comparison, runup is greatly influenced by bank slope angle, impact velocity, cliff mass, and height. The experimental results and developed prediction models can provide the basis for understanding the rotational cliff collapse-induced waves and can help with disaster mitigation and risk assessment by effectively predicting the wave amplitude and runup.

Keywords: Rotational cliff collapse, wave amplitude, runup, cliff fragmentation, prediction model.

1. Introduction

The phenomenon of cliff overturning is common along rivers and reservoirs (glacial lakes, recreational lakes), and has been captured by various people around the globe. The cliffs around these lakes are weathered due to climate change and wave action (Ró and Cerkowniak, 2024; Young et al., 2021) and can no longer be supported by the parent rock. When these initially intact, weathered cliffs fall into water, they usually fragment upon impact with the water surface, and as a result, induce an impulse water wave. Upon impact, the energy of gravitational mass is transferred to the water body, resulting in a huge splash and a wave train, propagating away from the point of impact. In the reservoirs and water channels located in mountainous regions, such as glacial lakes, dams, and a river flowing through valleys, these waves do not travel a long distance before reaching obstacles, opposite shores, or other infrastructure. As the waves retain most of their energy, size, and strength, the impact can cause significant damage to the population and infrastructure located along the banks of the reservoir. Historically, extreme impulse wave heights have been observed induced by landslides in events of 1958 Lituya Bay, USA, which caused a wave height of 524 m (Boultbee et al., 2006; Franco et al., 2020; Miller, 1960), 2007 Chehalis Lake, Canada, induced a wave of 38 m (Wang et al., 2015), 2015 Taan Fjord, USA, caused a wave of 193 m (Higman et al., 2018), and 2014 Lake Askaja (Gylfadóttir et al., 2017).

https://doi.org/10.5194/egusphere-2025-4396
Preprint. Discussion started: 23 September 2025

Moreover, the highly energetic gravity waves are capable of overtopping the dam wall, especially where the freeboard is just a few meters. The overtopping can result in dam failure and can lead to catastrophic events, such as caused by 1963 Vajont rock slide, in North Italy, where a 250 Mm^3 of rock mass slid into the dam reservoir and induced a huge wave that ran to a height of 200 m at the opposite bank (Franci et al., 2020; Heller and Ruffini, 2023; Ward, N. Steve and Day, Simon, 2011; Zhao et al., 2016), the resultant wave overtopped the dam and destroyed an entire village downstream. Similarly, in 2003 Qianjiangping landslide with a volume of 24 Mm^3, and in 2008 Gongjiafang landslide with a volume of 0.38Mm^3 in Three Gorges dam reservoir area induced a water wave that had an amplitude of 30 m and 32 m respectively (Wang et al., 2021), Gongjiafang landslide induced wave ran up to a height of 12.4 m on opposite bank (Huang et al., 2012).

These incidents highlight the need for predicting the subsequent energy transfer of such cliff collapses for disaster mitigation. The wave amplitude and runup height are of great importance. In contrast, the cases mentioned above are extreme; the small sliding, toppling, and falling events in small lakes and reservoirs can induce a wave of comparably small amplitude but capable of causing substantial damage to densely populated areas along the shoreline. Particularly, in the case of glacial lakes, recreational lakes, and lakes formed by previous landslides are prone to cause major disasters as they are considerably smaller compared to dam reservoirs (Gardezi et al., 2021). The phenomena of cliff overturning and falling are common around these lakes and have been captured by various people around the globe. Fig. 1 (a, b, and c) indicates a rotational (topple) cliff collapse in Furnas Lake, Brazil, on 8 January 2022, killing 10 people. As a result of the collapse, a huge splash and induced waves can be seen in Fig. 1 (c). Though scientists have analyzed the amplitude and runup of the waves induced by sliding masses, the literature lacks in providing detailed information on the formation and propagation of the wave induced by rotational cliff collapse. Moreover, the literature also lacks in elaborating on the shape of the induced splash. Effect of cliff fragmentation on the induced wave, as can be seen in Fig. 1 (a, b, and c), the falling cliff was still intact and broke under its own weight upon impact with the water surface

https://doi.org/10.5194/egusphere-2025-4396
Preprint. Discussion started: 23 September 2025

and induced a huge splash. Furthermore, though there are numerous prediction models available for the amplitude and runup of landslide-induced water waves, the prediction models for water waves induced by rotational fall of cliffs considering fragmentation are nonexistent.

Field data related to historical events is critical for disaster mitigation, but due to their occurrence in remote areas, the unavailability of measuring devices makes it difficult, leaving the physical modeling as the only source for understanding the wave generation, and propagation phenomena (Bellotti and Romano, 2017; Grilli et al., 2017; Takabatake et al., 2022; Wang et al., 2017a; Watts, 1998a). Previously, scientists have performed both two, and three-dimensional physical modeling for landslide induced water waves using either block slide (Heinrich, 1992; Heller and Spinneken, 2013; Najafi-Jilani and Ataie-Ashtiani, 2008; Sælevik et al., 2009), (M. Di Risio et al., 2009; Marcello Di Risio et al., 2009; Lindstrøm et al., 2014; Montagna et al., 2011; Panizzo et al., 2005; Wang et al., 2016) or granular slide (Fritz et al., 2003a, 2003b; Lindstrøm, 2016; Miller et al., 2016; Zweifel et al., 2006),(Heller and Spinneken, 2015; Huang et al., 2014; McFall and Fritz, 2016; Mohammed and Fritz, 2012; Romano et al., 2023). But none have developed a physical model to quantify the amplitude and runup of the waves induced by rotational cliff collapse, incorporating cliff fragmentation.

Along with the physical modeling, the wave generation and propagation phenomena have also been analyzed using numerical modeling by using Eulerian and Lagrangian methods, employing depth-averaged model, nonlinear shallow water, Navier-Stokes model, or Boussinesq equation, for both two- and three-dimensional modeling (Cecioni et al., 2011; Grilli et al., 2019; Heidarzadeh et al., 2020; Løvholt et al., 2005; Ruffini et al., 2019; Watts et al., 2003; Whittaker et al., 2017; Yavari and Ataie-Ashtiani, 2017). Moreover, numerous scientists have also used computational fluid dynamics (CFD) methods to analyze wave phenomena, just like experimental modeling, considering the sliding phase as solid material and water as the fluid phase (Abadie et al., 2010; Chen et al., 2020; Clous and Abadie, 2019; Franci et al., 2020b; Guan and Shi, 2023; Heller et al., 2016; Kim et al., 2020; Ma et al., 2015; Montagna et al., 2011; Mulligan et al., 2020; Paris et al., 2021; Rauter et al., 2022; Romano et al.,

https://doi.org/10.5194/egusphere-2025-4396
Preprint. Discussion started: 23 September 2025

2020; Shi et al., 2016).

Furthermore, scientists have also developed empirical prediction models for landslide-induced water waves by considering a combination of several parameters, i.e., geometric, geological, and kinematic characteristics of slides that contribute to wave generation, as shown in Table 1. Scientists have M. M. Das and Wiegel (1972) proposed that the velocity of the sliding material and water depth are the main components affecting the amplitude of the waves. Watts (1998) Stated that the slope angle, length, and mass of the slide are major factors influencing the amplitude of the wave. Fritz et al. (2003) stated that the landslide mass thickness mainly drives the amplitude of the induced wave. The empirical relations mentioned in Table 1 are mainly for the landslide-induced water waves, not for cliff collapse-induced water waves. Since this study is related to the wave induced by rotational cliff collapse, not the granular slide, the contributing parameters should also be different. Here in this study, we have considered seven parameters for developing a prediction model, i.e., water depth, fall height of the cliff, number of fragments, runup slope angle, height of the cliff, and impact velocity. In this study, we have incorporated a new parameter, i.e., the number of fragments, as the induced waves from fragments better replicate actual geohazard events.

Since the experimental and numerical models are expensive, laborious, time-consuming, and require a lot of expertise, to overcome these problems, there is a need for models that are quick and require less effort and cost. Consequently, the use of AI and ML-based models is gaining fame in the field of engineering. Previous prediction models for wave amplitude and runup employ simple regression analysis, which is insufficient for complex problems involving multiple parameters, but recently scientists have shifted towards more advanced ML models (Bujak et al., 2023; Cesario et al., 2024; Li et al., 2024, 2023a; Romano et al., 2009; Tarwidi et al., 2023; Tian et al., 2025; Wang et al., 2017b; Wiguna, 2022). Though scientists have used machine learning for wave amplitude and runup prediction modeling induced by various types of gravity flows, the prediction model for the waves induced by the rotational collapse of the cliff involving fragmentation is nonexistent to the authors' knowledge. Here in this study,

https://doi.org/10.5194/egusphere-2025-4396
Preprint. Discussion started: 23 September 2025

we have developed prediction models for wave amplitude and runup using genetic programming (GP).

GP-based models have recently gained traction for prediction, and multi-expression programming (MEP) and genetic-expression programming (GEP) are the most advanced, sophisticated, and widely used models. Both models are gene-type programming models that form tree-like models. These models are similar to living organisms, which can learn, adapt, and modify their composition, size, and shape (Gardezi et al., 2024; Usama et al., 2023). MEP is a cutting-edge, advanced form of GEP that adopts a demonstrative model for programming and uses linear chromosomes to determine optimum population size, mutation probability, and evolutionary model. Compared to other ML models, it can produce more precise results even when the problem complexity is unknown (Usama et al., 2023).

In this study, we have experimentally and numerically analyzed the hydrodynamics of the wave induced by rotational cliff collapse, and have also developed a prediction model for wave amplitude and runup. The physical modeling was carried out by developing a scaled water flume and a platform inducing rotational motion of the cliff. A total of 162 experiments were carried out by varying the seven control parameters, i.e., water depth, fall height, cliff mass, impact velocity, cliff height, runup slope angle, and number of fragments; for the sake of accuracy, each experiment was conducted twice, for consistency, thus making it 81 experiments. The parameters were selected to comprehensively elaborate on the distinct phases of rotational cliff collapse and induced waves. Water depth and runup slope angle provide the basis for wave propagation and runup. Whereas, the cliff collapse dynamics are explained by cliff mass (which governs the energy input), height of the cliff (defines the initial potential energy), and fall height (determines the transformation of potential to kinetic energy). Cliff impact velocity determines the amount of kinetic energy imparted to the water body at the time of impact, which is important for wave generation. Finally, the number of fragments is selected to demonstrate the effect of fragments of cliff upon impact with the water surface on wave amplitude and runup height. Together, these parameters define the energy budget from the state of rest to its release and then transfer to the water body to

https://doi.org/10.5194/egusphere-2025-4396
Preprint. Discussion started: 23 September 2025

its final stage as amplitude and runup. Since the wave velocity was not measured during the experiments, a 2D numerical model was developed using Ansys-Fluent, and wave velocity was measured; moreover, the results from the experiment were also cross-validated.

Finally, based on experimental results, prediction modeling for the amplitude and runup of water waves was carried out using multi-expression programming (MEP), and a novel prediction model was developed for the water waves induced by rotational cliff collapse, considering fragmentation of the cliff upon impact with the water surface.

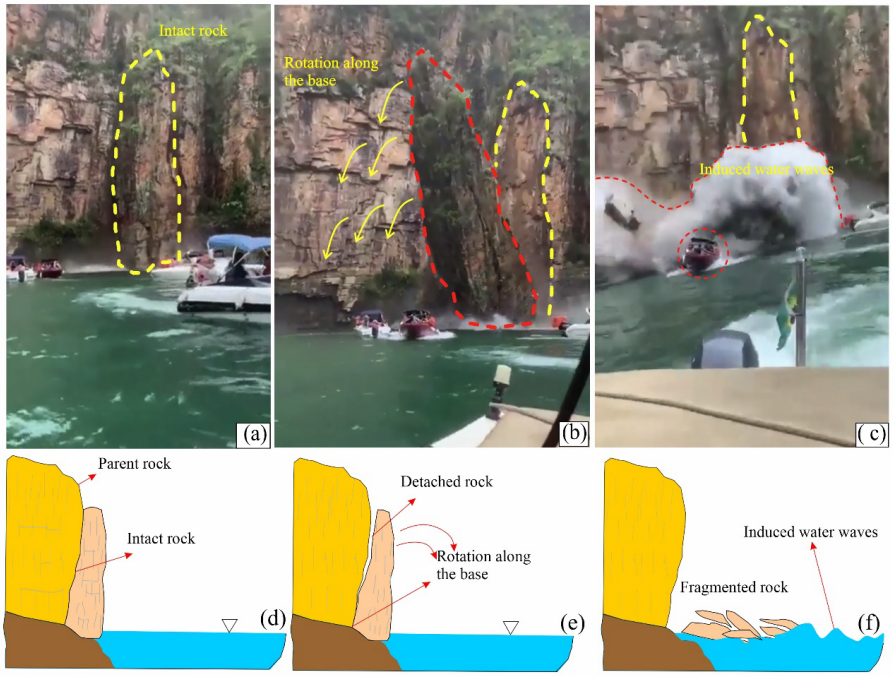

Fig. 1: (a, b, and c) waves induced by a cliff collapse in Lake Furnas, Brazil. (d, e, and f) sketch diagram indicating the detachment and rotational fall process.

Table 1: Historical overview of the prediction models for wave amplitude

Authors	Predictive model
Kamphuis and Bowering (1970)	$A_m = \left(\frac{v_s}{\sqrt{gh}}\right)^{0.7}\left(0.31 + 0.2\,log\left(\frac{l_s}{h^2}\right)\right) + 0.35e^{-0.08(x/h)}$
Noda (1970)	$A_m = 1.32\frac{v_s}{\sqrt{gh}}$
Huber and Hager (1997)	$\frac{H_m}{h} = 2 \times 0.88\,sin\,\theta\,cos^2\left(\frac{2\alpha}{3}\right)\left(\frac{\rho_5}{\rho_w}\right)^{0.25}\left(\frac{V}{wh^2}\right)^{0.5}\left(\frac{r}{h}\right)^{-\frac{2}{3}}$

https://doi.org/10.5194/egusphere-2025-4396
Preprint. Discussion started: 23 September 2025

Fritz et al. (2004)	$A_m = 0.25\left(\frac{v_s}{\sqrt{g_h}}\right)^{1\cdot4}\left(\frac{s}{h}\right)^{0.8}$
Panizzo et al. (2005)	$\frac{Hm}{h} = 0.07\left(\frac{T_s h^2}{ws}\right)^{-0.45}(sin\,\alpha)^{-0.88}e^{0.6cos^{\theta}}\left(\frac{r}{n}\right)^{-0.44}$
Heller (2007)	$A_m = \frac{4}{9}\left[F\left(\frac{s}{h}\right)^{1/2}\rho^{1/4}\left(cos\frac{6\alpha}{7}\right)^2\right]^{4/5}$
Mohammed and Fritz (2012)	$A_m = max(A_{C_1}, A_{C2})$ $A_{c1} = 0.3F^{2.1}\left(\frac{s}{h}\right)^{0.6}\left(\frac{r}{h}\right)^{\left(-1.2F^{0.25}\left(\frac{s}{h}\right)^{-0.02}w-0.33/h\right)}\cos\alpha$ $A_{c2} = 1.0FS^{0.8}\left(\frac{w}{h}\right)^{-0.4}\left(\frac{l}{h}\right)^{-0.5}\left(\frac{\gamma}{h}\right)^{-1.5F^{0.5}\left(\frac{w}{h}\right)^{-0.07}\left(\frac{w}{h}\right)^{-0.3}}cos^2\,\alpha$
Wang et al. (2016)	$A_m = 1.17F\left(\frac{sl}{bh}\right)^{0.25}\left(\frac{w}{b}\right)^{0.45}(\mathrm{Sin}^2\alpha + 0.6\cos^2\alpha)$
Li et al. (2023)	$A_m = 0.59\sqrt{\frac{2H(1-fcot\alpha)}{h}}\left(\frac{swl}{h^3}\right)^{N^{-0.11}}\left(\frac{x}{h}\right)^{-0.43}\cos^2\left(\frac{2}{3}\alpha\right)$
Note: *Note*: l is the landslide length; s is the landslide thickness; w is the landslide width; m is the landslide mass weight; V is the landslide volume; H is the landslide height; b is the river width; h is the still water depth; $x(r)$ is the offshore distance from the bank slope; α is the slope angle; θ is the angular direction; vs is the impact velocity.	

2. Research methodology

2.1 Model Preparation

The physical modeling for wave amplitude and runup induced by rotational cliff collapse was carried out in a three-dimensional water flume made up of plexiglass, as shown in Figs. 2 and 3. One end of the flume is vertical at 90°, whereas the other end is inclined and fixed at 30° (Fig. 3a and b). The flume is 0.55 m high, 0.5 m wide, and 1.4 m long along the base and 2.35 m long at the top. Furthermore, to measure the runup of induced water waves at various slope angles, two sliding rails were installed towards the inclined end at 45° and 60°. So, upon insertion of the gate at 45°and 60°, the top length of the flume was further reduced according to the Pythagoras theorem. To induce the rotational cliff collapse, a 0.55 m wide and 0.6 m high movable platform was prepared, which can move in the vertical direction and can also rotate about its axis. The flume was marked with a vertical scale to measure the water depth.

https://doi.org/10.5194/egusphere-2025-4396
Preprint. Discussion started: 23 September 2025

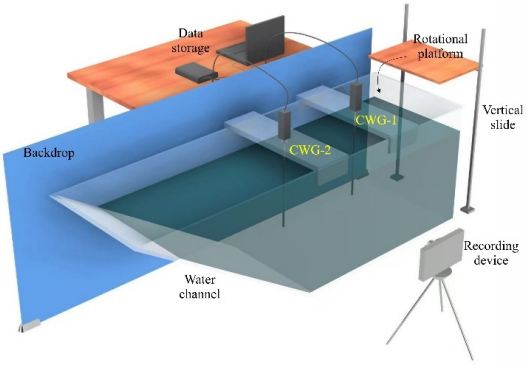

Fig. 2: Illustration of experimental setup including wave gauges, rotational platform, recording, and data storage devices.

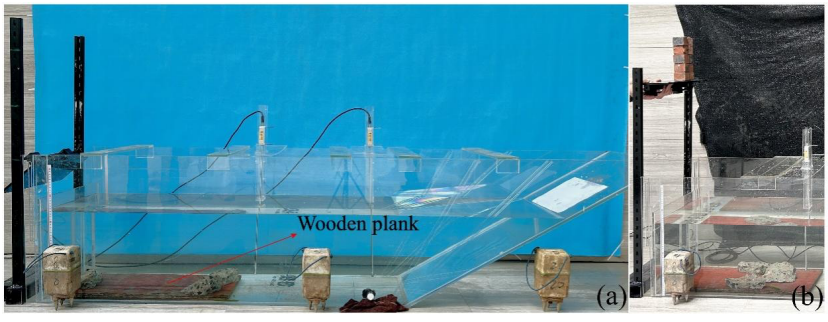

Fig. 3: Photographs of the setup, (a) Experimental flume, (b) platform for inducing rotational cliff collapse.

2.2 Test preparation and materials

Physical experiments were carried out by varying the water depth, fall height, number of fragments, bank slope angle, mass of falling rock, cliff height, and impact velocity. The tests were carried out for three water depths, i.e., 0.34 m, 0.27 m, and 0.20 m, and three fall heights, i.e., 0.64 m, 0.44 m, and 0.245 m from the surface of the water level. Furthermore, the number of blocks was also varied, i.e., 6, 10, and 12 blocks having combined weights of 1.445 kg, 2.29 kg, and 2.82 kg, respectively. At the same time, the impact velocity changed by changing the fall height. The wave runup was measured by varying the bank slope angle, i.e., 30°, 45°, and 60°.

To replicate the field density of the rocks, red gutka bricks having a density of around 2000 kg/m^3 were used. The single block had a dimension of 0.55 x 0.05 x 0.042

https://doi.org/10.5194/egusphere-2025-4396
Preprint. Discussion started: 23 September 2025

m. A combination of 6, 10, and 12 blocks of red gutka bricks were used to form a cliff and measure the wave amplitude and runup of induced waves, the blocks were joined together with the help of cement paste having water cement ratio W/C 0.8 and cured for 2 hours Infront of an electric heater, such that the bond is weak enough that it fragments at the joints upon impacting the water surface. The bonded blocks were placed on the rotational platform at specific heights, i.e., 0.64 m, 0.44 m, and 0.245 m from the water level, and were allowed to rotate under their own weight by pulling the hinge, such that the placed block falls in the water following rotation motion along its base Fig. 3 (b). To avoid the slippage of blocks and to replicate field conditions, fine-grained bricks of the same material as the cliff were pasted on the rotational platform. Furthermore, to reduce the impact of falling blocks on the base of the flume, a wooden plank weighing 2.69 kg and dimensions 0.65m x 0.37m x 0.01 m was placed at the point of impact inside the flume. Due to its large surface area and lighter density, it tends to float in the flume, so two blocks of concrete weighing 3.58 kg were placed on it, Fig. 3 (a).

The induced wave amplitude was measured by placing the wave measuring gauges at a distance of 0.65 m and 0.135 m from the vertical face; the gauges were wired and connected to the laptop. At the same time, the runup was measured manually with the help of a scale by pasting a scaled paper on the slope. Furthermore, the experiments were also recorded with the help of a high-resolution camera for verification purposes.

2.3 Numerical Modeling

Simulating multi-phase flows is challenging due to the constant deformation of the liquid-gas interface. Various numerical methods have been developed to model these flows, each offering unique advantages depending on the specific flow regime and characteristics of interest. In this study, the Volume of Fluid (VOF) method is utilized for its effectiveness in handling significant interface distortions and topological changes. The VOF method offers superior mass conservation, which is critical in high velocity impact conditions where liquid fragmentation and wave generation are significant (Brackbill et al., 1992; Hirt and Nichols, 1981). Other approaches provide superior

https://doi.org/10.5194/egusphere-2025-4396
Preprint. Discussion started: 23 September 2025

accuracy in modeling interfaces and surface tension, but they struggle to manage complex scenarios (Liu and Liu, 2010; Monaghan, 1994; Yang and Kong, 2018). Given these trade-offs, the Volume of Fluid (VOF) method finds an optimal balance of computational efficiency, interface tracking capability, and proven reliability for modeling multiphase flow in the moderate-to-high velocity range relevant to this study. Therefore, a two-dimensional numerical model of a cliff, having the same properties as the experimental cliff mentioned previously, hitting the water surface is developed using the VOF method to accurately capture the liquid-gas interface.

In this approach, a volume fraction (α), ranging between 0 and 1, is applied across the entire computational domain. A value of $\alpha = 1$ indicates a control volume filled with liquid, while $\alpha = 0$ denotes a control volume filled with gas. The interface is represented by values where $0 < \alpha < 1$. In the Volume of Fluid (VOF) method, the momentum equation is solved across the entire computational domain, with the resulting velocity field shared by all phases. To account for surface tension effects, a continuum surface force (CSF) model is employed (Backbill et al., 1992). The normal vector $\boldsymbol{n}$ and interface mean curvature $\boldsymbol{\kappa}$ are as follows, respectively:

$$n = \frac{\nabla \alpha}{/\nabla \alpha/} \tag{1}$$

and

$$\kappa = \nabla . \frac{\nabla \alpha}{/\nabla \alpha/} \tag{2}$$

The interface is maintained as sharp through the use of geometric reconstruction to ensure its clarity. The volume fraction (α) is discretized with the geo-reconstruct scheme, while the convective terms in the momentum equation are handled using a second-order upwind method. The PISO (Pressure-Implicit with Splitting of Operators) algorithm was employed for pressure-velocity coupling, which is well-suited for transient flows. Temporal discretization employs a second-order implicit scheme, and spatial gradients are calculated using the Least Squares Cell-Based method.

To have an accurate simulation of the rotational motion of the cliff through the air-water interface in a multi-phase flow environment, dynamic meshing was implemented within the ANSYS Fluent framework. This approach facilitated the adaptation of the

https://doi.org/10.5194/egusphere-2025-4396
Preprint. Discussion started: 23 September 2025

computational mesh to accommodate the cliff's movement while maintaining the integrity of the liquid-gas interface captured by the Volume of Fluid (VOF) method. Dynamic meshing was critical for modeling the complex interactions between the falling cliff and the surrounding air and water phases, allowing the mesh to deform and adapt in response to the cliff's trajectory. In ANSYS Fluent, the dynamic meshing strategy employed a combination of mesh deformation and local remeshing techniques to handle the cliff's motion. Mesh deformation was applied to adjust the existing mesh nodes smoothly as the cliff moved, preserving mesh quality in regions experiencing moderate displacement. For areas near the cliff where significant deformation could lead to poor mesh quality, local remeshing was utilized to regenerate mesh elements for better numerical stability and accuracy. The smoothing and remeshing algorithms were configured to maintain high mesh quality, with a skewness threshold set to prevent excessive element distortion.

The rotational cliff collapse was simulated using an in-house user-defined function (UDF). This UDF interfaced with ANSYS Fluent to dynamically update the rock's position and velocity. To enhance computational efficiency, a dynamic mesh zone was defined around the cliff, with a finer mesh resolution near its surface to capture the sharp gradients in the flow field and interface dynamics. The mesh was gradually coarsened away from the rock to reduce computational cost while maintaining sufficient resolution in the far-field regions. The dynamic meshing process was synchronized with the transient flow solver, using a time step size determined through a time step independence study to balance accuracy and computational efficiency.

2.4 Multi-expression programming

The MEP model was developed for predicting wave amplitude and runup using experimental data, as shown in Table 2. A dataset of 81 experiments was prepared by alternately varying seven different parameters, and the results for wave amplitude and runup were recorded. Furthermore, the data was divided into 70/30 ratios for training and validation purposes before developing the model. The model starts working by generating a random chromosome population, and it continues to generate the chromosomes until a terminal condition is achieved, generating an optimal expression

https://doi.org/10.5194/egusphere-2025-4396
Preprint. Discussion started: 23 September 2025

from the data having input and output pairs over a certain number of generations, as shown in Fig. 4.

Based on a binary tournament process, parents are selected and then undergo a recombination process through a consistent crossover probability. This recombination produces two more offspring. These offspring go through mutation, and if these offspring perform better than the least fitting offspring in the current population, then the better offspring replace them. The illustrations used by MEP are similar to the ones used by C++ and Pascal compilers. The MEP chromosomes are comprised of numerous genes combined using various mathematical operators such as addition (+), subtraction (-), multiplication (x), and division (/), and these genes create expression trees (ETs) (Cheng et al., 2020). Moreover, there are several parameters such as code length, sub-population size and number, crossover probability, and other sets of various functions involved in in generation of MEP code, and they also govern the overall performance of the code. Among these parameters, the size of the population tells us about the number of programs being generated, whereas an increase or decrease in subpopulation size directly affects the complexity and computation time of the model. Moreover, the length of the developed model is controlled by varying the code length parameter.

Table 2: Input parameters and corresponding wave amplitude and runup heights.

S/No.	Water depth (d)	Drop height (H)	Fragments (N_f)	Angle (α)	Cliff Mass(m)	Cliff height(h)	Velocity (v)	Amplitude (A)	Runup (m)
1	0.34	0.245	6	30	1.445	0.12	2.19	0.0225	0.051
2	0.34	0.445	6	30	1.445	0.12	2.95	0.0230	0.056
3	0.34	0.645	6	30	1.445	0.12	3.56	0.0365	0.068
4	0.34	0.245	6	45	1.445	0.12	2.19	0.0370	0.045
5	0.34	0.445	6	45	1.445	0.12	2.95	0.0425	0.051
.	.	.	.	.	.	.	.	.	.
.	.	.	.	.	.	.	.	.	.
.	.	.	.	.	.	.	.	.	.
37	0.27	0.245	10	30	2.295	0.20	2.19	0.0431	0.116
38	0.27	0.445	10	30	2.295	0.20	2.95	0.0510	0.129
39	0.27	0.645	10	30	2.295	0.20	3.56	0.0685	0.141
40	0.27	0.245	10	45	2.295	0.20	2.19	0.0390	0.085
41	0.27	0.445	10	45	2.295	0.20	2.95	0.0523	0.102
.	.	.	.	.	.	.	.	.	.
.	.	.	.	.	.	.	.	.	.

https://doi.org/10.5194/egusphere-2025-4396
Preprint. Discussion started: 23 September 2025

.	.	.	.	.	.	.	.	.	.
78	0.2	0.645	12	45	2.82	0.24	3.56	0.0733	0.146
79	0.2	0.245	12	60	2.82	0.24	2.19	0.0565	0.062
80	0.2	0.445	12	60	2.82	0.24	2.95	0.0636	0.083
81	0.2	0.645	12	60	2.82	0.24	3.56	0.0657	0.098

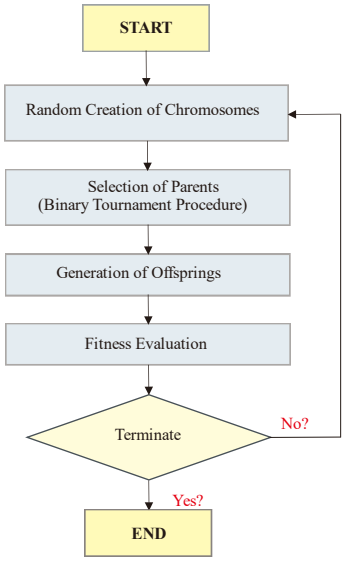

Fig. 4 MEP flowchart

3. Results and discussions

3.1 Experimental results

The experimental results of the wave amplitude and runup, induced by rotational cliff collapse, reveal complex hydrodynamic processes. As shown in Fig. 5, the failure is initiated by the rotational fall of the cliff, leading to a significant amount of impact energy upon hitting the water surface. The impact induced a huge splash, which is evident from Fig. 5 (b, e & h). It was observed that the shape of the splash also varies with water depth for all the cases; higher water depths resulted in a mushroom-shaped splash, i.e., broader on the top, as can be seen in Fig. 5(h). The observed phenomena perfectly align with the basic concepts of fluid dynamics, which state that greater depths absorb more impact energy compared to shallow waters. Shallow waters produced a vertically elongated splash as can be seen in Fig. 5 (b & e). It can be observed that as the depth decreases, the splash becomes more elongated, and this is due to the fact that shallower depths intensify the upward momentum transfer, thus resulting in a more

https://doi.org/10.5194/egusphere-2025-4396
Preprint. Discussion started: 23 September 2025

elongated shape (Kubota and Mochizuki, 2009).

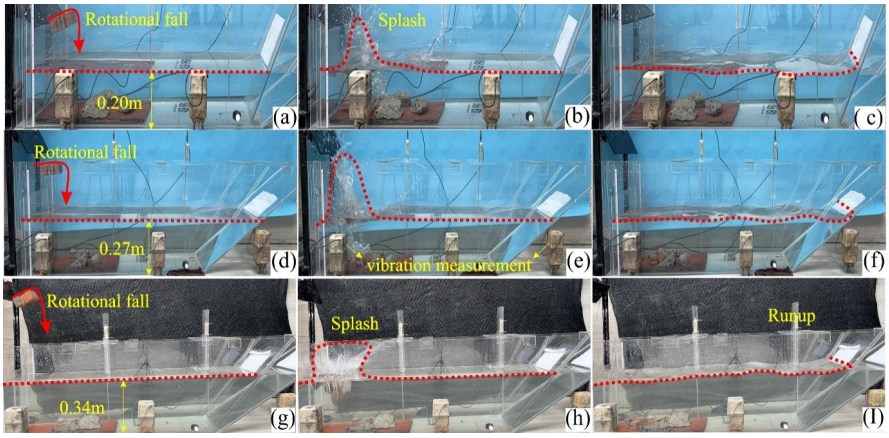

Fig. 5: A pictorial display of the experimental setup for various water depths, i.e., 0.20 m, 0.27m, and 0.34 m. (a, d & g) indicate rotational fall of the cliff, (b, e & h) showing splash as a result of cliff impact, (c, f & I) formation and propagation of induced wave and runup at various slope angles.

3.1.1 Relation between energy and amplitude

Further, the relationship between impact energy and wave response was also investigated by establishing a dimensionless impact energy parameter ($K.E/\rho gh^3$). Where $K.E$ is the kinetic energy of the cliff, ρ is the density, and h is the water depth. The negative quadratic coefficient in Fig. 6(a) indicates a nonlinear response, such that at the start, the wave amplitude increases as the impact energy increases, but later it decreases, due to reduced energy transfer at higher impact values. Moreover, the coefficient of determination was found to be 77% indicating a good data fit.

Moreover, the results for the relative wave amplitude and wave energy were analyzed for three water depths, i.e., 0.34 m, 0.27 m, and 0.20 m., as shown in Fig. 6(b). The results indicate a strong correlation for all three cases, with coefficients of determination around 0.96. The results indicate a direct relation between wave height and energy, whereas the decreasing slope values with the increasing water depth suggest that for deeper water the wave amplitude decreases at a slower rate with increasing wave energy, thus highlighting the impact of water depth on the wave dynamics, such that shallower water allows more amplification of waves for the same

https://doi.org/10.5194/egusphere-2025-4396
Preprint. Discussion started: 23 September 2025

energy level, and this is due to the increased non-linear interactions and enhanced energy concentrations in shallower depths (Myrhaug and Lader, 2019).

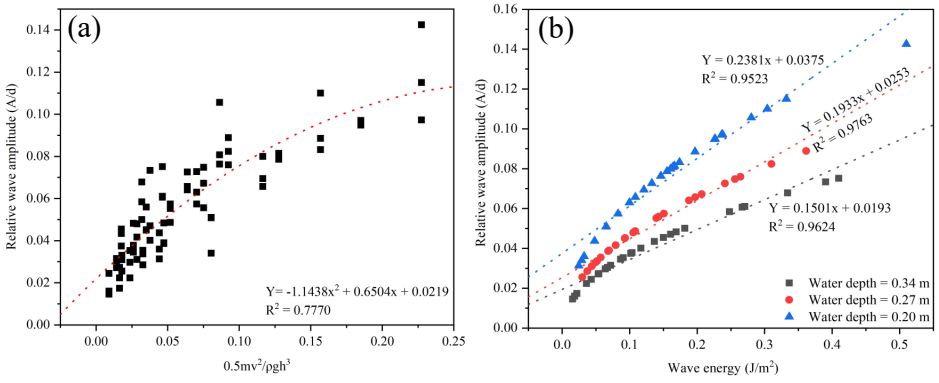

Fig. 6: (a) Impact energy vs relative wave amplitude, (b) Wave energy vs relative wave amplitude

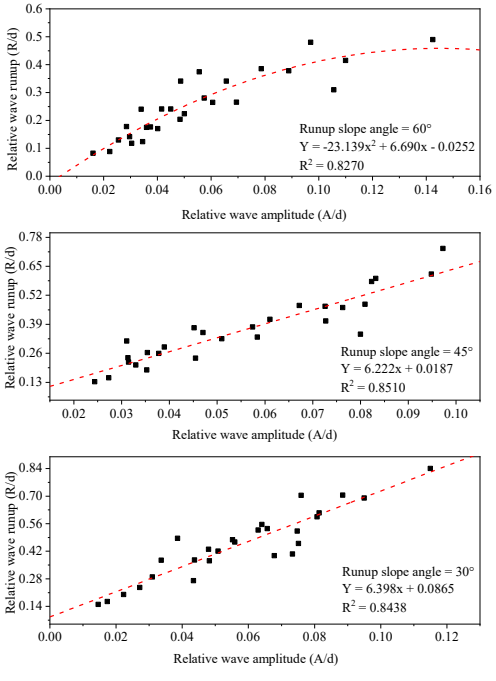

Fig. 7: Relative wave amplitude vs relative wave height.

The results for the relative wave height and runup for all three water depths and three runup slope angles are shown in Fig. 7. The relationship indicates a strong correlation between wave amplitude and runup for all three slope angles. The

https://doi.org/10.5194/egusphere-2025-4396
Preprint. Discussion started: 23 September 2025

decreasing line-slope values with increasing runup slope angle indicate that wave runup increases at a slower rate for sharp slope angles compared to mild slopes. The trend highlights the effect of slope angle on the runup. The result also indicates that the mild slope angles help wave runup amplification, as they dissipate a very small amount of energy, whereas steeper angles result in lower runup heights because of higher energy losses (Wu et al., 2018).

3.1.2 Impact Froude no vs Relative wave amplitude

Fig. 8 indicates the relationship between the impact Froude number and relative wave amplitude (A/d), under varying experimental conditions for the first gauge, i.e., near the impact zone. Since we are interested in the immediate response of the wave influenced by the impact Froude number. The results indicate that as the water depth decreases, the relative wave amplitude and impact Froude number increase, indicating a reduction in the dissipation of impact energy, causing pronounced surface turbulence and increased wave height. Additionally, the decreased water depth also increased the value of the impact Froude number by reducing its characteristic velocity, resulting in stronger wave generation upon impact. The calculations for Reynolds number for the experiments resulted in very high values, thus indicating a strong turbulent flow, which is also evident from Fig. 5, so viscous effects are very, very small and can be ignored, thus indicating the Froude dynamics similarity. The experimental results indicate the complex interaction between wave propagation, impact dynamics, and bathymetrical effects in waves induced by rotational cliff collapse. Moreover, upon impact, the cliff fragmentation distributes impact energy over a larger area of water, thus increasing wave height by enhanced turbulence and water splashing effects.

https://doi.org/10.5194/egusphere-2025-4396
Preprint. Discussion started: 23 September 2025

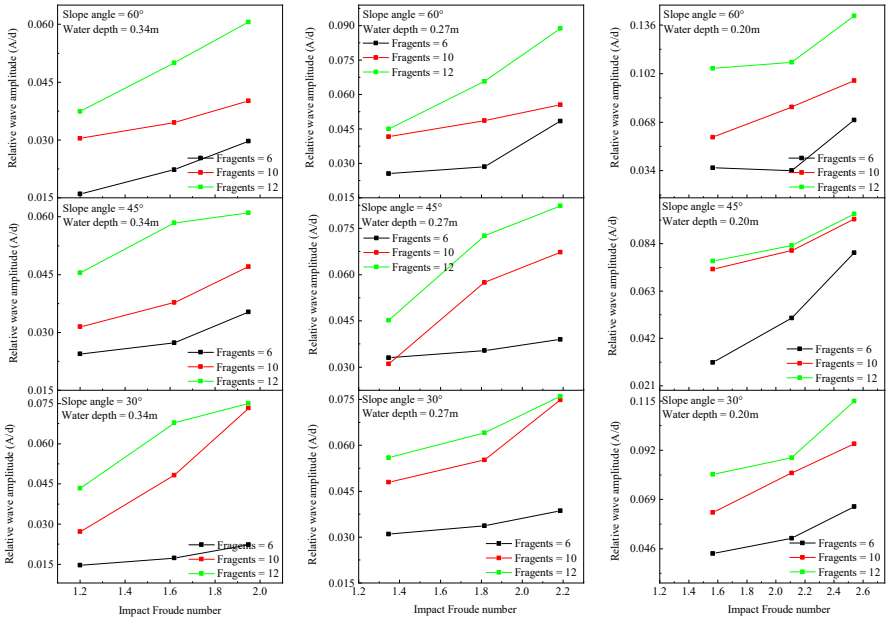

Fig. 8: Relationship between impact Froude number and relative wave height

3.1.3 Wave amplitude results

The results for the wave amplitude for various parameters are shown in Figs. 9, 10, and 11. As mentioned earlier, two gauges were used to measure the induced wave amplitude. Fig. 9 provides a detailed comparison of the wave amplitude recorded at both gauges for 60°runup slope angle and a 0.445m fall height. It can be observed that gauge-1, which is near to impact zone, has a higher relative amplitude compared to gauge-2. Furthermore, the results for the relative wave amplitude against the normalized time were also analyzed for all the water depths (0.20m, 0.27m, and 0.34m), fall height (0.245m, 0.445m, and 0.645m), and cliff height (0.12m, 0.20m, and 0.24m). The results indicate that the wave amplitude increases as the cliff height, impact velocity, and number of fragments increase for all the water depths, as can be observed in Fig. 10, thus demonstrating that the potential energy of the falling cliff plays a critical role in the magnitude of the resulting wave.

Interestingly, comparing the wave amplitude induced by cliffs of various heights falling from the same height revealed that the water depth and the wave have an inverse

https://doi.org/10.5194/egusphere-2025-4396
Preprint. Discussion started: 23 September 2025

relationship. As shown in Fig. 10 (a, b, and c), the average wave amplitude for various cliff heights and the same fall height of 0.245 m at 0.20m water depth is 26% more than the average wave amplitude induced by 0.27m water depth and 50% more than the 0.34m water depth wave amplitude. Similarly, Fig. 10 (d, e, and f) indicates that the average wave amplitude for 0.445m fall height at 0.20m water depth is 18% more than 0.027 m and 47% more than 0.34 m water depth, whereas, for 0.645m fall height wave amplitude induced by 0.20 m water depth is 25% more than 0.27m and 37% more than 0.34m water depth (Fig. 10 g, h & i), thus suggesting that the deeper water dissipates the impact energy more effectively, as the deep water have more mass available to absorb and redistribute the impact energy, compared to shallower water thus reducing the overall amplitude of the induced wave. Moreover, a similar trend was observed for the wave amplitude involving 45°and 60°runup slope angle.

Later on, we performed another experiment by using granular material of equivalent mass as of cliff and slid it on a 30° slope, for all the water depths, and amplitude of the induced wave was measured as shown in Fig. 11. Fig. 11(a) indicates that the wave amplitude for 0.20 m water depth and 1.445kg granular mass (equivalent to 0.12 m cliff height) was 15% more than 0.27m water depth and 65% more than wave amplitude induced by 0.34 m water depth. Whereas for 2.29kg and 2.82kg granular mass equivalent to 0.20 m and 0.24 m cliff height similar trend was observed as shown in Fig. 11 (b and c), thus indicating that as the water depth increases, the wave amplitude decreases for all the equivalent granular masses as happened in the case of cliff fall.

Furthermore, a comparison between the wave amplitude induced by a falling cliff and equivalent granular mass at various water depths indicates that the amplitude of the wave induced by an equivalent granular mass in 0.34m, 0.27m, and 0.20m water depth was on average 28%, 35% and 42% less than the wave amplitude induced falling cliff. The substantial difference in wave amplitude highlights the importance of energy transfer in wave formation. The falling cliff following a rotational motion imparts a more sudden and concentrated impact that allows an efficient energy transfer to water, leading to higher wave amplitudes. On the other hand, granular flows, being more deformable and flowing along a slope, result in gradual energy transfer over a wide area,

https://doi.org/10.5194/egusphere-2025-4396
Preprint. Discussion started: 23 September 2025

thus resulting in lower wave amplitudes. The results highlight that it's not only the total impact energy that affects the behavior of the induced wave, but the mode of energy transfer also plays a critical role (Mohammed and Fritz, 2012; Wunnemann and Weiss, 2015). Based on the experimental results for wave amplitude and runup induced by rotational cliff collapse that fragments upon impact with the water surface, a novel prediction model was prepared using multi-expression programming. The justifications for the use of MEP have been well explained in the previous sections.

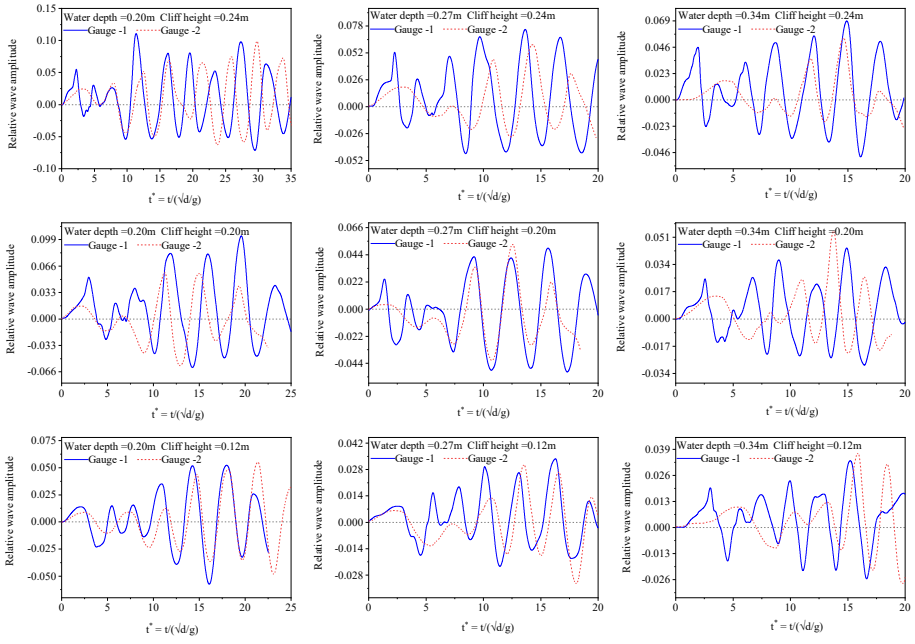

Fig. 9: A comparative display of the wave recorded at gauge 1&2 for a 60° slope angle, and 0.445 m fall height.

https://doi.org/10.5194/egusphere-2025-4396
Preprint. Discussion started: 23 September 2025

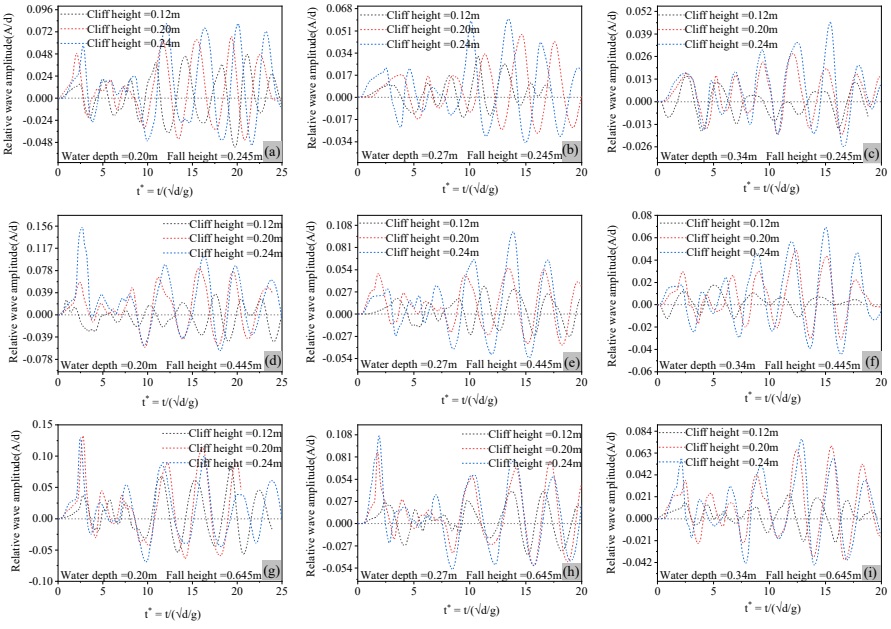

458

459 Fig. 10: Relative wave amplitude for various water depths, cliff height, and fall height
460 at 30°runup slope angle, (a, b&c) relative wave amplitude induced by 0.245m fall
461 height, (d, e&f) relative wave amplitude induced by 0.445m fall height, (g, h&i)
462 relative wave amplitude induced by 0.645m fall height.

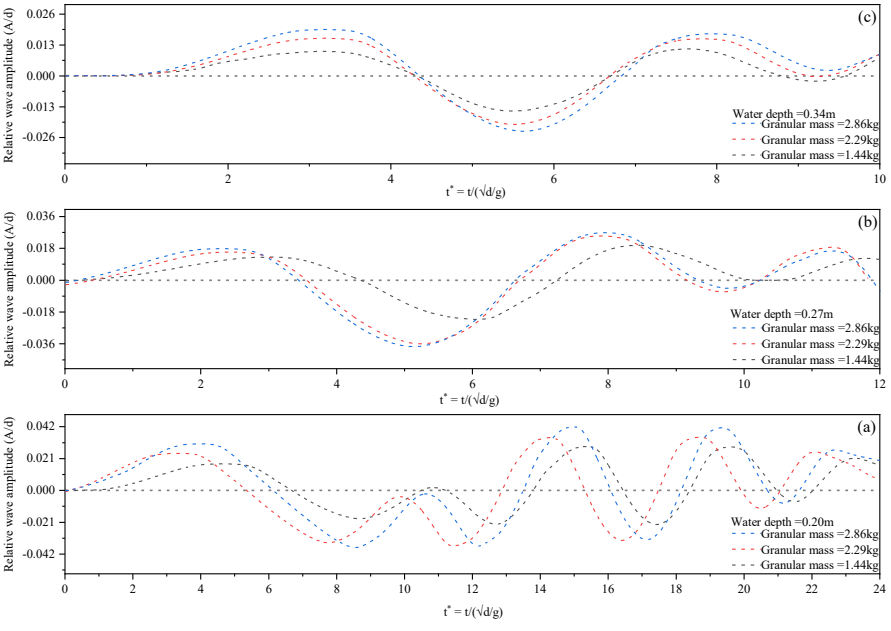

463

464 Fig. 11: Wave induced by equivalent granular mass

https://doi.org/10.5194/egusphere-2025-4396
Preprint. Discussion started: 23 September 2025

3.2 Numerical modeling results

The numerical simulations conducted in this study successfully captured key dynamic characteristics of the wave generated by the rotational cliff collapse, specifically the wave amplitude and wave runup, across a range of test cases. Moreover, the front velocity of the incident wave was also measured. The simulations were also focused on verifying the results obtained from the rotational cliff collapse in the experiments. To quantify the wave amplitude, runup, and velocity, a post-processing technique was employed. To establish the reliability of the wave front velocity measurements, the velocity was calculated at 5–7 distinct locations along the wave's propagation path and at multiple time steps during the simulation. This multi-point sampling approach minimized errors due to spatial and temporal variations. Fig. 12 shows a representative case of wave formation and propagation in a water tank at a depth of d = 0.2 m at various time frames.

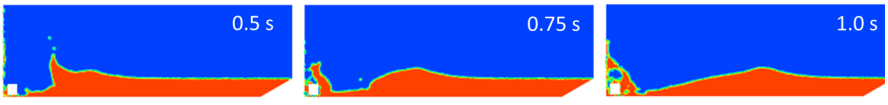

Fig. 12 Wave formation and propagation at water depth of d = 0.2 m at various time frames.

The wave amplitude was defined as the peak vertical displacement of the liquid surface relative to the undisturbed free surface level. Fig. 13 illustrates a representative case, depicting the wave front propagation.

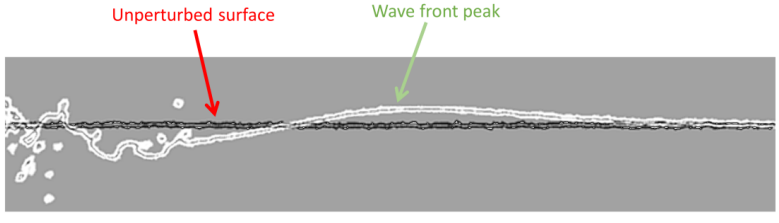

Fig. 13 Wave dynamics following a rotational cliff collapse in water depth d = 0.34 m. Stable liquid surface before impact (black line); wave front propagating to the right (white line).

To validate the results of simulations, we compared the results of the runup height with the experimental values. Table 3 presents the runup values for various

https://doi.org/10.5194/egusphere-2025-4396
Preprint. Discussion started: 23 September 2025

runup slope angles, i.e., 30°, 45°, and 60°, for a water depth of d=0.27m. The comparison of simulated values was performed at this depth, as it lies in the middle of the experimental test range of water depths. Numerical modeling results indicate that for a fixed water depth, the runup values consistently decrease as the runup slope angle increases from 30° to 60°. At a water depth of d=0.27 m, the runup decreases from 0.2 m at 30° to 0.17 m at 45°, and further to 0.11 m at 60°. This reduction is attributed to the changing momentum transfer dynamics with increasing slope angle. At less steep angles (closer to horizontal, e.g., 30°), the rock's momentum generates a stronger radial splash and greater upslope displacement of the liquid along the cliff. As the angle increases toward 60°, a larger component of the momentum is directed parallel to the cliff, reducing the vertical impulse. The experimental and numerical results agree well, and the difference lies within the acceptable range of 4-5%. The experimental results for the other two water depths also indicate similar behavior.

Table 3: Peak runup values along the various slope angles at a water depth of d=0.27m

Depth d (m)	**Numerical-30°**	**Exp-30°**	**Numerical-45°**	**Exp-45°**	**Numerical-60°**	**Exp-60°**
0.27	0.20	0.19	0.17	0.16	0.11	0.102

Next, we measured the wave velocity through the numerical results, as it wasn't captured accurately through experimental images. Fig. 14 illustrates the simulated wave fronts at a time instant of t =1 second following the impact of the solid rock on the liquid pool, for various water depths and a fixed slope angle of 30 degrees. These visualizations highlight the propagation of the waves from the impact zone. The slope angle was varied across simulations to assess its influence on wave characteristics. It was observed that changes in the slope angle induced only minor variations in both the wave front velocity and wave amplitude for a given pool depth. These perturbations were typically within 1–2% of the mean values. Consequently, to streamline the analysis and focus on dominant trends, the wave front velocity and height were averaged over the range of slope angles for each specific water depth.

However, variations in water depth exerted a pronounced effect on the wave

https://doi.org/10.5194/egusphere-2025-4396
Preprint. Discussion started: 23 September 2025

dynamics, leading to significant alterations in both the propagation velocity and amplitude of the generated waves. This depth-dependent behavior is quantified in Table 4, which presents the averaged results from the numerical simulations. For a shallow water depth of d=0.2 m, the average wave front velocity was computed as 1.48 m/s, with a corresponding average wave height of 0.11 m. As the pool depth increased to d=0.27 m, the velocity rose to 1.58 m/s, while the wave height decreased to 0.07 m. Further deepening to d=0.34 m yielded a velocity of 1.74 m/s and a reduced wave height of 0.06 m. These trends indicate an approximately linear increase in velocity with depth, accompanied by an inverse relationship for wave amplitude.

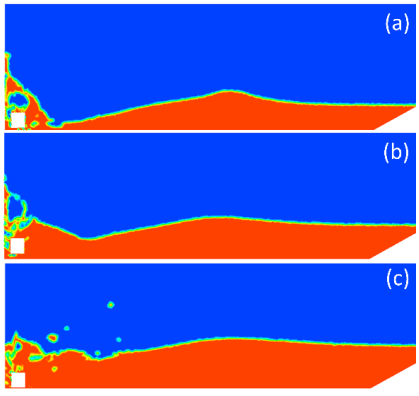

Fig. 14 Propagating wave fronts after the impact at time t = 1 s for a slope angle of 30-degree. (a) d = 0.2 m, (b) d = 0.27 m, (c) d = 0.34 m.

The observed depth dependence can be rationalized through fundamental principles of wave propagation in gravity-dominated, multi-phase flows. In the shallow water regime, given that the pool depths (0.2–0.34 m) are comparable to or smaller than the wavelengths of the generated waves, the phase velocity c of long gravity waves approximates $c \approx \sqrt{gh}$, where g is the gravitational acceleration (9.81 m/s²) and h is the undisturbed water depth. This relation arises from the shallow water equations, where hydrostatic pressure balance and negligible vertical acceleration dominate, leading to a dispersionless incident wave speed that scales with the square root of depth. Substituting the water depths yields theoretical velocities of approximately 1.40 m/s for d=0.2 m, 1.63 m/s for d=0.27 m, and 1.83 m/s for d=0.34 m, which align closely with the simulated values (discrepancies of 7–10% may stem from viscous dissipation, non-

https://doi.org/10.5194/egusphere-2025-4396
Preprint. Discussion started: 23 September 2025

hydrostatic effects near the impact zone, or spreading of the wave front). A comparative analysis of the results is shown in Table 4.

Conversely, the decrease in wave amplitude with increasing water depth aligns with energy conservation and volume displacement considerations in impact-generated waves. The impact of rotational cliff collapse imparts a fixed kinetic energy and displaces a finite volume of liquid, creating an initial cavity and subsequent outflow that evolves into a propagating wave. In shallower pools, the displaced volume is confined to a smaller cross-sectional area, resulting in greater vertical amplification to accommodate the same mass redistribution. For deeper water depths, the energy is distributed over a larger water column, diluting the surface perturbation and yielding lower amplitudes. The trends observed in the numerical simulations for water waves induced by rotational cliff collapse are in good agreement with theoretical and experimental results, indicating that water depth has a direct effect on the wave velocity and an inverse effect on the wave amplitude and runup.

Table 4**:** The average wave propagation velocity and amplitude for various water depths.

Water depth *d* (m)	**Avg. wave velocity *v* (m/s)**	**Theoretical wave velocity *c* (m/s)**	**Wave amplitude (m)**
0.2	1.48	1.40	0.11
0.27	1.58	1.63	0.07
0.34	1.74	1.83	0.06

3.3 MEP model results

The purpose was to develop a precise model for wave amplitude and runup induced by rotational cliff collapse. The predicted model is a function of seven variables, i.e., water depth, fall height, cliff mass, impact velocity, cliff height, runup slope angle, and number of fragments, and can be described as follows,

$$Wave\ amplitude\ and\ runup\ = f\left(d, H, m, v, h, \alpha, N_f\right) \quad (3)$$

The relation among the parameters was evaluated using Pearson's correlation to analyze the multicollinearity and interdependency between the parameters, as they can

https://doi.org/10.5194/egusphere-2025-4396
Preprint. Discussion started: 23 September 2025

obscure the interpretation of the developed model. The model was developed by splitting the data into two subsets, i.e., training (70%) and testing (30%). The randomization was done by MEP itself. Following the criteria, 70% of the data, i.e., 57 data points, were taken as training data, whereas 30% of the data, i.e., 24 data points, were considered for validation of the model. The mathematical expression for MEP is obtained by solving the C++ code and representing it as per optimized hyperparameter settings, as shown in Table 5. The prediction model for wave amplitude and runup was developed by analyzing the MEP code in MATLAB, as shown in Equations 4 and 5.

Table 5: Parametric settings of the MEP algorithm for wave amplitude and runup

Sr.No.	Parameters	Wave amplitude	Wave runup
1	Number of sub-populations	125	85
2	Sub-population size	115	75
3	Crossover probability	0.85	0.60
4	Code length	35	25
5	Tournament size	30	10
6	Mutation probability	0.085	0.06
7	Number of generations	250	120
8	Crossover type	Uniform	Uniform
9	Error measure	Mean absolute error	Mean absolute error
10	Problem type	Regression	Regression
11	Function set	+, -, x, /, ^	+, -, x, /, ^
12	Terminal set	Problem Input	Problem Input
13	Operators	0.5	0.5
14	Simplified	Yes	Yes
15	Variables	0.5	0.5
16	Random seed	0	0
17	Constants	0	0

$$Wave\ amplitude\ A = d^{\left(\frac{\alpha}{d(d+N_f+m)}\right)} + \frac{2vh^2}{m+N_f+d(d+N_f+m)} + 2vhd^{\left(\frac{\alpha}{d(d+N_f+m)}\right)} \quad (4)$$

$$Wave\ runup\ R = \frac{A\left(h+\left(A\cdot\left(d-\frac{B}{\alpha}\right)\right)^{B/\alpha}\right)^{A}\cdot B}{\alpha} \quad (5)$$

$$A = v + h^d$$

$$B = v + m + h^d$$

Whereas d is the water depth (m), m is the mass of the cliff (kg), v is the impact velocity (m/s), h is the cliff height (m), α is the runup slope angle, and N_f is

https://doi.org/10.5194/egusphere-2025-4396
Preprint. Discussion started: 23 September 2025

the number of fragments.

3.3.1 Prediction performance of the developed model

The robustness of the proposed model was evaluated by comparing it with well-established statistical indices, i.e., mean absolute error (MAE), root mean square error (RMSE), correlation coefficient (Cr), Nash–Sutcliffe efficiency (NSE), and performance index (PI). The indices can be represented by equation (6-10) (Alavi et al., 2010; Khan et al., 2022).

$$MAE = \frac{\sum_{i=1}^{n}|e_i - p_i|}{n} \tag{6}$$

$$RMSE = \frac{\sum_{i=1}^{n}(e_i - p_i)^2}{n} \tag{7}$$

$$NSE = 1 - \frac{\sum_{i=1}^{n}(e_i - p_i)^2}{\sum_{i=1}^{n}(e_i - \bar{e}_i)^2} \tag{8}$$

$$PI = \frac{RRMSE}{1+R} \tag{9}$$

$$R^2 = \left(\frac{\sum_{i=1}^{n}(e_i - \bar{e}_i)(p_i - \bar{p}_i)}{\sum_{i=1}^{n}(e_i - e_i)^2 \sum_{i=1}^{n}(P_i - \bar{P}_i)^2} \right)^2 \tag{10}$$

Whereas, $\bar{e}_i$ and $\bar{p}_i$ are the average values of the experimental and predicted results, and e_i and p_i are i_{th} values of the modeled and predicted results, for n total samples. It is good to consider the error indices while analyzing the predictive capability of complex models. The wave runup model demonstrated a robust performance for both training and testing datasets. The lower values of RMSE and MAE indicate little deviation from experimental values, while RSE and RMSE values confirm lower normalized error, as shown in Table 6. The higher values of NSE and Cr further validated the model reliability for the training phase. Whereas for the validation dataset, i.e., the unseen data model displays even stronger performance with lower RMSE and MAE values compared to the training dataset. Moreover, higher Cr and lower performance index values highlight enhanced model efficiency. This suggests that the model works well for unseen data, making it suitable for predicting the wave runup induced by rotational cliff collapse (Gardezi et al., 2024).

The predictive performance of the wave amplitude model in the case of training data demonstrated a strong correlation with high R^2 values and low RMSE and MAE

https://doi.org/10.5194/egusphere-2025-4396
Preprint. Discussion started: 23 September 2025

values corresponding to 13.14% relative error, thus suggesting a good agreement between experimental and predicted values, as shown in Table 6. The higher NSE and C_r values further confirmed the model's reliability for the training dataset with minimal systematic bias. When the model was exposed to unseen data, it still maintained reasonable accuracy with an R^2 value of 0.78. Though the values of error matrices, i.e., RMSE, MAE, and RRMSE, are a bit higher than the training data set, this is expected due to inherent generalization challenges. Similarly, the higher NSE and C_r values, though lower than the training dataset, indicate consistent predictive performance of the wave amplitude model with little increase in bias. Overall model exhibited strong predictive performance in the training and testing phase, with a little expected decline in the validation phase.

Table 6: Performance index values for MEP-based velocity prediction model.

Performance parameters	Wave Amplitude		Wave Runup	
	Training data	Validation data	Training data	Validation data
RSQ	0.8823	0.7811	0.8748	0.9691
RMSE	0.00178	0.0025	0.01327	0.00617
MAE	0.00135	0.00176	0.0108	0.00504
RSE	0.1180	0.2439	0.1306	0.0312
RRMSE	0.1314	0.1594	0.1472	0.0660
P. index	0.0698	0.0908	0.076	0.0333
NSE	0.8819	0.7560	0.8693	0.9687
C_r	0.9393	0.8829	0.9353	0.9844

Previously, scientists have also used the slope of the regression line as a performance indicator for AI models, thus representing a correlation between experimental and predicted results. Fig. 15 (a & b) shows the regression line for our wave amplitude and runup model. For wave amplitude, the slope value for the training data set is 0.88, which is adequate, and 0.78 in validation, which is still greater than the minimum value of 0.7; it can happen as the model involving numerous parameters and complex phenomena usually performs slower for the unseen data(Yarkoni and Westfall, 2019). Whereas, for wave runup, the model performed very well for both training and validation data sets with an R^2 value of 0.87 and 0.96, respectively.

https://doi.org/10.5194/egusphere-2025-4396
Preprint. Discussion started: 23 September 2025

The accuracy of the proposed model can also be checked using residual error plots, which are obtained by subtracting experimental and predicted values (Alavi et al., 2013). The results indicate that the amplitude model has minimum and maximum values of -0.004 m and 0.0065 m, as shown in Fig. 16 (a), whereas for wave runup the minimum and maximum values are -0.01875 and 0.024 (Fig. 16b). Moreover, it can also be observed that error values are populated along the x-axis, therefore, showing low error frequency, and accuracy of both the models.

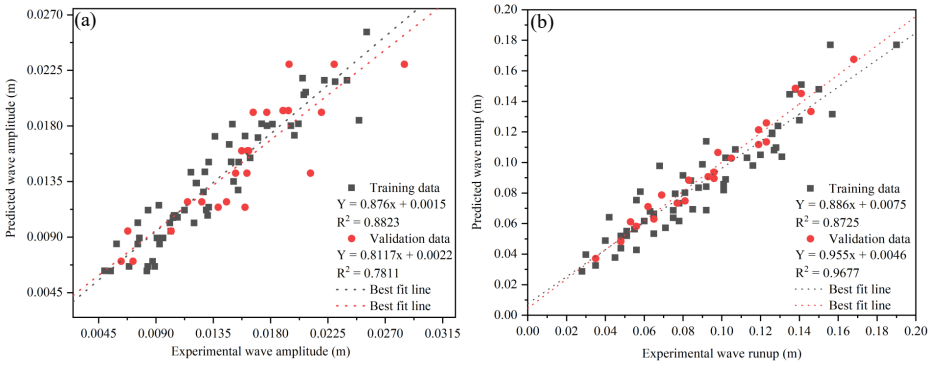

Fig. 15 Tracing the experimental results by predicted values, (a) wave amplitude and (b) wave runup

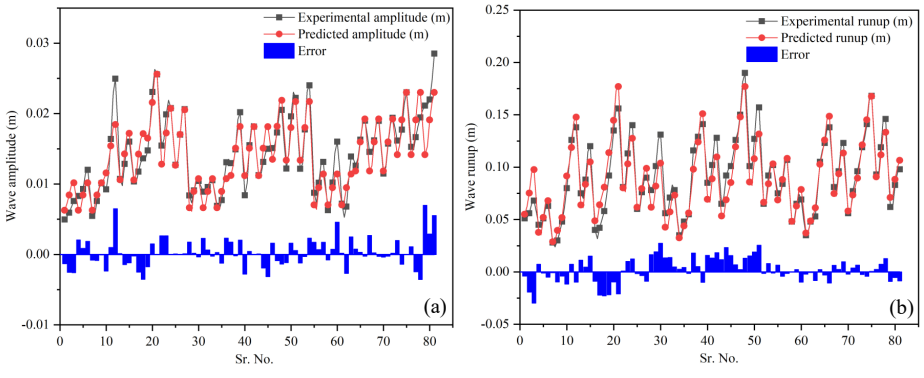

Fig. 16 Indicating error values between experimental and predicted model (a) wave amplitude, and (b) Wave runup

3.2 Validation of the developed model

The validation of the proposed model is an important feature in predictive modeling. It has been observed that sometimes the model performs very well for training data sets,

https://doi.org/10.5194/egusphere-2025-4396
Preprint. Discussion started: 23 September 2025

but fails to perform during the validation stage for unseen data. So, the developed prediction model was further validated by conducting the sensitivity and parametric analysis for both the wave amplitude and runup.

3.2.1 Sensitivity analysis

Sensitivity and parametric analysis play a vital role in determining the robustness of the proposed model. The sensitivity analysis (SA) of the developed prediction model for the entire dataset tells us how sensitive the model is to any changes in input parameters. So for an independent parameter Y_i the SA can be calculated using equations 11 and 12, which indicates that for any parameter, the values were varied between two extremes and others were constant to their average, and the outcome was found in the form of Y_i, and then the same process was repeated for all the remaining parameters.

$$R_k = f_{max}(Y_k) - f_{min}(Y_k) \tag{11}$$

$$Relative\ Importance\ \ SA\ (\%) = \frac{R_k}{\sum_{n}^{j=1} R_j} \times 10 \tag{12}$$

Whereas, $f_{max}(Y_k)$ and $f_{min}(Y_k)$ represent the minimum and maximum values of the model-based results grounded on the *kth* domain of the input parameters in the above equation. Fig. 17 (a & b) shows the results of the sensitivity analysis of the developed prediction model for the wave amplitude and runup. Figure 17 (a) indicates that the wave amplitude is greatly influenced by the height of the cliff *(h)* and has an effect of almost 51%. The water depth (d) contributes 4.36% to wave amplitude, cliff mass (m) contributes 4.69%, and impact velocity (v) and number of fragments (N_f) contributes 18% and 22% to the induced wave amplitude. Whereas the fall height (H) and runup slope angle (α) do not affect the wave amplitude. Since the impact velocity parameters have already catered for the fall height that's why it is not visible in the proposed model. The model tells us that impact velocity, cliff height, and number of fragments contribute approximately 90% to the wave amplitude induced by the rotational fall of the cliff. It can be concluded that the effect of $h > N_f > v > m > d$ on the induced wave amplitude.

Similarly, the sensitivity analysis of wave runup (Fig. 17b) indicates that runup is

https://doi.org/10.5194/egusphere-2025-4396
Preprint. Discussion started: 23 September 2025

greatly influenced by bank slope angle (α) and has an effect of 34%. Impact velocity (v) contributes 25.3%, cliff mass (m) 20.3%, cliff height (h) 13.3%, and water depth (d) contributes around 7% to wave runup. Whereas, the number of fragments and fall height that have already been catered in impact velocity don't contribute to wave runup. This suggests that wave runup is primarily governed by coastal geometry, i.e., bank slope angle and cliff height, and hydrodynamic forces, i.e., impact velocity, whereas water depth contributes a little to wave runup. It can also be concluded as the effect of $\alpha > v > m > h > d$ on the induced wave amplitude.

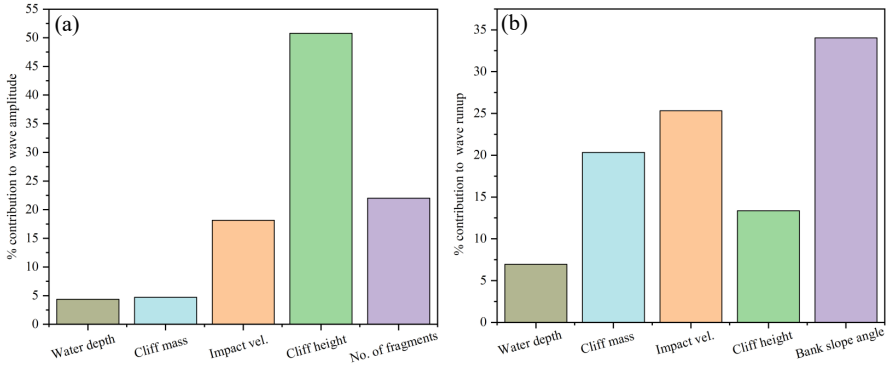

Fig. 17 Sensitivity analysis of the MEP-based wave amplitude and runup model

3.2.2 Parametric Analysis

Parametric analysis results for the input parameters for the wave amplitude used in this study are displayed in Fig. 18. The parametric analysis indicates that wave amplitude decreases as the water depth, number of fragments, and cliff mass increase, whereas it increases with the increase in cliff height and impact velocity. These trends are in line with the fundamental physics principles (Bougouin et al., 2020; Lipiejko et al., 2023)– deep waters dissipate more energy, and greater impact velocities and larger cliff heights impart more kinetic and potential energies to water bodies for wave generation. Whereas, the inverse relation between the number of fragments and wave amplitude proposes a potential threshold effect in which initial fragmentation contributes to wave formation, whereas excessive fragments contribute to energy dissipation owing to increased turbulence. The sensitivity analysis further quantified the effect of these parameters, classifying cliff height as a major contributing factor in

https://doi.org/10.5194/egusphere-2025-4396
Preprint. Discussion started: 23 September 2025

wave amplitude variations, followed by impact velocity, number of fragments, water depth, and mass of cliff. The strong influence of cliff height indicates its direct effect in determining the potential energy for wave generation. Moreover, the larger sensitivity value of fragments regardless of their inverse parametric relation shows a complex relation, where fragment count plays a considerable but context-dependent role in wave generation and propagation. The dominance of cliff height, impact velocity, and fragment count suggests that these parameters should be prioritized in future prediction models. These findings are important for developing predictive models for wave generations due to rotational cliff collapse.

The developed model for wave amplitude provides valuable insights into fundamental physics governing wave formation and propagation induced because of rotational cliff collapse. The strong height dependence of the model confirms the classical principle of conservation of potential energy, whereas the fragment count dependence reveals energy partitioning mechanisms. The results of performance indices and sensitivity, and parametric analysis increase our understanding of how geometric and dynamic characteristics govern the wave characteristics, with relevance to hazard assessment and disaster mitigation in coastal regions prone to cliff collapse following rotational motion.

The results of the parametric analysis for wave runup are presented in Fig. 19. It can be observed from Fig. 19 (a & e) that as the water depth and bank slope angle increase, the wave runup decreases, due to energy dissipation and different wave breaking dynamics. Conversely, as the cliff mass, cliff height, and impact velocity increase, the wave runup increases, as greater kinetic energy and inertia impart greater uprush. Notably, all the parameters present a strong correlation with the runup (more than 97%), highlighting their statistical significance. The results agree with the general physics laws, where mild slopes and larger impact forces result in higher runups, whereas deep waters attenuate wave energy.

An important observation from parametric analysis of wave amplitude and runup, as shown in Fig. 18b, and 19c, indicates that cliff mass represents a nonlinear relation with wave amplitude and a linear relation with runup. This is due to the fact that the

https://doi.org/10.5194/egusphere-2025-4396
Preprint. Discussion started: 23 September 2025

variations in wave amplitude are governed by a nonlinear energy dissipation, where hydrodynamic forces follow a quadratic dependence on the velocity. In the case of light cliff collapses, the dynamic responses result in complex absorption and distribution, whereas heavier cliff collapses promote wave reflection along with nonlinear effects of wave breaking and splash-induced turbulence, as can be observed in Fig. 5 (b, e&h). Conversely, the wave runup exhibits a linear relation with cliff mass, and this is due to the law of conservation of momentum, such that the resisting inertial force is directly proportional to cliff mass. The greater resistance to motion of heavier cliffs allows more energy to be conserved and utilized for higher wave runups before dissipation. The main difference between the two trends is that the wave amplitude is controlled by localized energy losses, whereas runup is governed by bulk momentum transfer rather than localized losses.

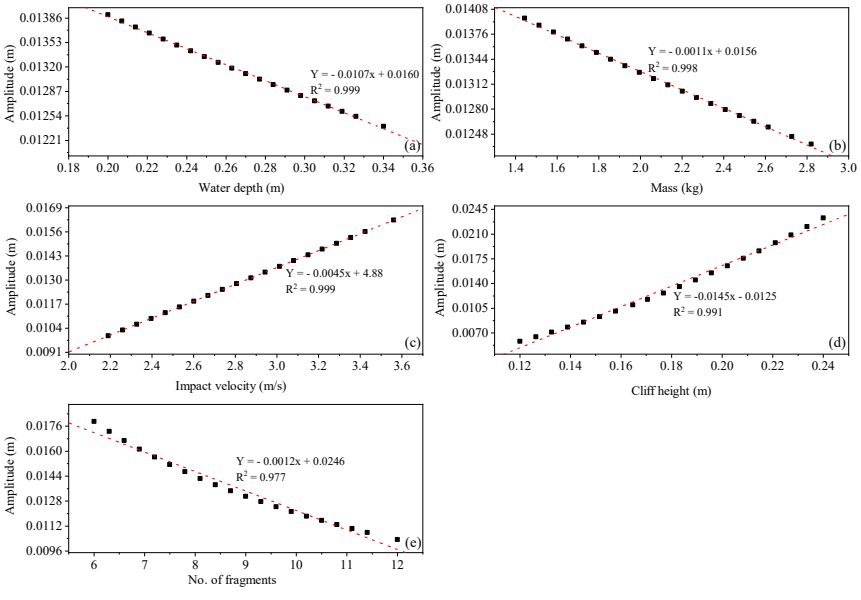

Fig. 18 Parametric analysis for wave amplitude (a) water depth, (b) cliff mass, (c) impact velocity, (d) cliff height, (e) number of fragments.

https://doi.org/10.5194/egusphere-2025-4396
Preprint. Discussion started: 23 September 2025

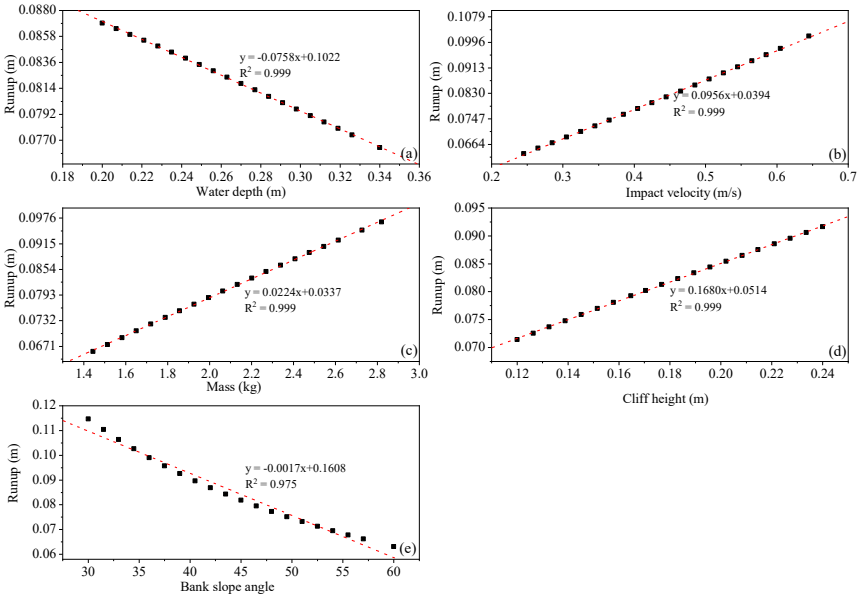

Fig. 19 Parametric analysis for wave runup (a) water depth, (b) impact velocity, (c) mass of the cliff, (d) cliff height, (e) bank slope angle.

4. Conclusions

While designing wave protection structures along the banks of reservoirs, it is common to use the empirical relations developed for granular flows, i.e., landslides and avalanches, to predict the amplitude and runup of the waves. However, the waves induced by various types of slides behave differently and should be treated accordingly. The dynamics of the waves induced by falling cliffs are entirely different from the waves induced by continuous granular flows. Similarly, the dynamics of the waves induced by falling cliffs following different types of motion (translational, rotational) are also different. This study aimed to develop a novel wave amplitude and runup prediction model for waves induced by rotational fall of the cliff using a combination of seven governing parameters, and then compare it with the dynamics of the wave induced by continuous granular flows. Based on the results and discussions, the study concludes as follows,

1. It was concluded that the shape of the induced splash depends on water depth; increased depth forms a mushroom-shaped splash, whereas shallow water forms a

https://doi.org/10.5194/egusphere-2025-4396
Preprint. Discussion started: 23 September 2025

vertically elongated splash. Moreover, shallow water allows more amplification of waves for the same energy level compared to deep water.

2. The effect of viscous forces is very, very small and can be ignored, since the Reynolds number for all the experiments is very high, thus leaving the Froude number as the best possible dynamic scaling factor. It is concluded that the Froude number also increases as the water depth decreases.
3. The study concludes that wave amplitude is greatly influenced by cliff height, impact velocity, and the number of fragments. For all the cases, the deep water dissipated more energy compared to shallow waters, thus resulting in lower amplitudes.
4. The amplitude of the wave induced by equivalent granular mass is lower than the waves induced by rotational cliff collapse, thus concluding that the mode of energy transfer to the water body plays a critical role in wave dynamics.
5. A second-level validation of the developed model was performed by conducting sensitivity and parametric analysis. It is concluded that the amplitude is highly sensitive to any change in cliff height, impact velocity, and number of fragments. In contrast, runup greatly depends on runup slope angle, impact velocity, and mass of the cliff.

Funding

This work was supported by the National Key R&D Program of China (Grant No. 2023YFC3007001), the China Postdoctoral Science Foundation (Grant no. 2024M762420), the National Natural Science Foundation of China (Grant no. 42202312), and the Fundamental Research Funds for the Central Universities.

Declarations

Competing interests: The authors declare no competing interests.

References

Alavi, A.H., Gandomi, A.H., Nejad, H.C., Mollahasani, A., Rashed, A., 2013. Design equations for prediction of pressuremeter soil deformation moduli utilizing

https://doi.org/10.5194/egusphere-2025-4396
Preprint. Discussion started: 23 September 2025

739 expression programming systems. Neural Comput. Appl. 23, 1771–1786.
740 https://doi.org/10.1007/s00521-012-1144-6

741 Alavi, A.H., Gandomi, A.H., Sahab, M.G., Gandomi, M., 2010. Multi expression
742 programming: A new approach to formulation of soil classification. Eng. Comput.
743 26, 111–118. https://doi.org/10.1007/s00366-009-0140-7

744 Bellotti, G., Romano, A., 2017. Wavenumber-frequency analysis of landslide-
745 generated tsunamis at a conical island. Part II: EOF and modal analysis. Coast.
746 Eng. 128, 84–91. https://doi.org/10.1016/j.coastaleng.2017.07.008

747 Bougouin, A., Paris, R., Roche, O., 2020. Impact of Fluidized Granular Flows into
748 Water : Implications for Tsunamis Generated by Pyroclastic Flows. J. Geophys.
749 Res. Solid Earth 1–17. https://doi.org/10.1029/2019JB018954

750 Boultbee, N., Stead, D., Schwab, J., Geertsema, M., 2006. The Zymoetz River rock
751 avalanche, June 2002, British Columbia, Canada. Eng. Geol. 83, 76–93.
752 https://doi.org/10.1016/j.enggeo.2005.06.038

753 Brackbill, J.U., D.B. Kothe, and C. Zemach, *A continuum method for modeling surface*
754 *tension.* Journal of computational physics, 1992. 100(2): p. 335-354.

755 Bujak, D., Ilic, S., Miliˇ, H., 2023. Wave Runup Prediction and Alongshore Variability
756 on a Pocket Gravel Beach under Fetch-Limited Wave Conditions. J. Mar. Sci. Eng.

757 Cesario, E., Giampá, S., Baglione, E., Cordrie, L., Selva, J., Talia, D., 2024. Machine
758 Learning for Tsunami Waves Forecasting Using Regression Trees. Big Data Res.
759 36, 100452. https://doi.org/10.1016/j.bdr.2024.100452

760 Das, M.M., Wiegel, L.., 1972. Waves Generated by Horizontal Motion of a Wall. J.
761 Waterw. Harb. costal Eng. Div. 98.

762 Franci, A., Cremonesi, M., Perego, U., Crosta, G., Oñate, E., 2020. 3D simulation of
763 Vajont disaster. Part 1: Numerical formulation and validation. Eng. Geol. 279.
764 https://doi.org/10.1016/j.enggeo.2020.105854

765 Franco, A., Moernaut, J., Schneider-Muntau, B., Strasser, M., Gems, B., 2020. The
766 1958 Lituya Bay tsunami - Pre-event bathymetry reconstruction and 3D numerical
767 modelling utilising the computational fluid dynamics software Flow-3D. Nat.
768 Hazards Earth Syst. Sci. 20, 2255–2279. https://doi.org/10.5194/nhess-20-2255-
769 2020

770 Fritz, H., Hager, W., Minor, H., 2004. Near field characteristics of landslide generated
771 impulse waves. J Waterw. Port Coast. Ocean Eng. 130, 287–302.

https://doi.org/10.5194/egusphere-2025-4396
Preprint. Discussion started: 23 September 2025

Fritz, H.M., Hager, W.H., Minor, H.E., 2003. Landslide generated impulse waves. 1. Instantaneous flow fields. Exp. Fluids 35, 505–519. https://doi.org/10.1007/s00348-003-0659-0

Gardezi, H., Bilal, M., Cheng, Q., Xing, A., Zhuang, Y., Masood, T., 2021. A comparative analysis of attabad landslide on january 4, 2010, using two numerical models. Nat. Hazards 107, 519–538. https://doi.org/10.1007/s11069-021-04593-0

Gardezi, H., Ikrama, M., Usama, M., Iqbal, M., Jalal, F.E., Hussain, A., Li, X., 2024. Predictive modeling of rutting depth in modified asphalt mixes using gene-expression programming (GEP): A sustainable use of RAP, fly ash, and plastic waste. Constr. Build. Mater. 443, 137809. https://doi.org/10.1016/j.conbuildmat.2024.137809

Grilli, S.T., Shelby, M., Kimmoun, O., Dupont, G., Nicolsky, D., Ma, G., Kirby, J.T., Shi, F., 2017. Modeling coastal tsunami hazard from submarine mass failures: effect of slide rheology, experimental validation, and case studies off the US East Coast. Nat. Hazards 86, 353–391. https://doi.org/10.1007/s11069-016-2692-3

Gylfadóttir, S.S., Kim, J., Helgason, J.K., Brynjólfsson, S., Höskuldsson, Á., Jóhannesson, T., Harbitz, C.B., Løvholt, F., 2017. The 2014 Lake Askja rockslide-induced tsunami: Optimization of numerical tsunami model using observed data. J. Geophys. Res. Ocean. 122, 4110–4122. https://doi.org/10.1002/2016JC012496

Heller, V., 2007. Landslide Generated Impulse Waves: Prediction of Near Field Characteristics (Doctoral dissertation, Eth Zurich).

Heller, V., Ruffini, G., 2023. A critical review about generic subaerial landslide-tsunami experiments and options for a needed step change. Earth-Science Rev. 242, 104459. https://doi.org/10.1016/j.earscirev.2023.104459

Higman, B., Shugar, D.H., Stark, C.P., Ekström, G., Koppes, M.N., Lynett, P., Dufresne, A., Haeussler, P.J., Geertsema, M., Gulick, S., Mattox, A., Venditti, J.G., Walton, M.A.L., McCall, N., Mckittrick, E., MacInnes, B., Bilderback, E.L., Tang, H., Willis, M.J., Richmond, B., Reece, R.S., Larsen, C., Olson, B., Capra, J., Ayca, A., Bloom, C., Williams, H., Bonno, D., Weiss, R., Keen, A., Skanavis, V., Loso, M., 2018. The 2015 landslide and tsunami in Taan Fiord, Alaska. Sci. Rep. 8, 1–12. https://doi.org/10.1038/s41598-018-30475-w

Hirt, C.W. and B.D. Nichols, *Volume of fluid (VOF) method for the dynamics of free boundaries.* Journal of computational physics, 1981. **39**(1): p. 201-225.

Huang, B., Yin, Y., Liu, G., Wang, S., Chen, X., Huo, Z., 2012. Analysis of waves generated by Gongjiafang landslide in Wu Gorge, three Gorges reservoir, on

https://doi.org/10.5194/egusphere-2025-4396
Preprint. Discussion started: 23 September 2025

November 23, 2008. Landslides 9, 395–405. https://doi.org/10.1007/s10346-012-0331-y

Huber, A., Hager, W., 1997. Forecasting impulse waves in reservoirs, in: Proc 19th Congrès Des Grands Barrages, Florence, ICOLD, Paris. pp. 993–1005.

Kamphuis, J., Bowering, R., 1970. Kamphuis JW, Bowering RJ (1970) Impulse waves generated by landslides, in: Proc 12th Coastal Eng 1:575–588, ASCE, Washing Ton, USA.

Khan, K., Ashfaq, M., Iqbal, M., Khan, M.A., Amin, M.N., Shalabi, F.I., Faraz, M.I., Jalal, F.E., 2022. Multi Expression Programming Model for Strength Prediction of Fly-Ash-Treated Alkali-Contaminated Soils. Materials (Basel). 15. https://doi.org/10.3390/ma15114025

Kubota, Y., Mochizuki, O., 2009. Splash Formation by a Spherical Body Plunging into Water. J. Vis. 12, 339–346.

Li, Y., Ding, Y., Yang, L., Liu, X., Liu, Y., 2023a. A prediction model for the rockslide-generated wave amplitude under the condition of bedrock mass breakup. Ocean Eng. 272, 113845. https://doi.org/10.1016/j.oceaneng.2023.113845

Li, Y., Ding, Y.N., Yang, L., Liu, X.S., Liu, Y., 2023b. A prediction model for the rockslide-generated wave amplitude under the condition of bedrock mass breakup. Ocean Eng. 272. https://doi.org/10.1016/j.oceaneng.2023.113845

Li, Y., Peng, T., Xiao, L., Wei, H., Li, X., 2024. Wave runup prediction for a semi-submersible based on temporal convolutional neural network. J. Ocean Eng. Sci. 9, 528–540. https://doi.org/10.1016/j.joes.2022.08.005

Lipiejko, N., Whittaker, C.N., Lane, E.M., Power, W.L., 2023. Wave Generation by Fluidized Granular Flows : Experimental Insights Into the Maximum Near-Field Wave Amplitude. J. Geophys. Res. Ocean. https://doi.org/10.1029/2022JC019583.

Liu, M. and G. Liu, *Smoothed particle hydrodynamics (SPH): an overview and recent developments.* Archives of computational methods in engineering, 2010. 17: p. 25-76.

Miller, D.J., 1960. Giant waves in Lituya Bay, Alaska. Geol. Surv. Prof. Pap. No. 354 C ; US Governement Print. Off. Washington, DC, USA 51–86.

Mohammed, F., Fritz, H.M., 2012a. Physical modeling of tsunamis generated by three-dimensional deformable granular landslides. J. Geophys. Res. Ocean. 117, 1–20. https://doi.org/10.1029/2011JC007850

https://doi.org/10.5194/egusphere-2025-4396
Preprint. Discussion started: 23 September 2025

Mohammed, F., Fritz, H.M., 2012b. Physical modeling of tsunamis generated by three-dimensional deformable granular landslides. J. Geophys. Res. 117. https://doi.org/10.1029/2011JC007850

Monaghan, J.J., *Simulating free surface flows with SPH.* Journal of computational physics, 1994. **110**(2): p. 399-406.

Myrhaug, D., Lader, P.F., 2019. Random wave-induced current in shallow water using deep water wind and wave statistics. Marit. Eng. 174, 1–20.

Noda, E., 1970. Water waves generated by landslides. J Water Port Coast. Ocean Div, Am Soc Civ Eng. 96, 835–855.

Panizzo, A., De Girolamo, P., Petaccia, A., 2005. Forecasting impulse waves generated by subaerial landslides. J. Geophys. Res. Ocean. 110, 1–23. https://doi.org/10.1029/2004JC002778

Ró, G., Cerkowniak, G., 2024. Soft postglacial cliffs in Poland under climate change. oceanologia 66. https://doi.org/10.1016/j.oceano.2024.01.003

Romano, M., Romano, M., Liong, S., Vu, M.T., Zemskyy, P., Doan, C.D., Dao, M.H., Tkalich, P., 2009. Artificial neural network for tsunami forecasting. J. Asian Earth Sci. 36, 29–37. https://doi.org/10.1016/j.jseaes.2008.11.003

Sohag, M., et al., *Numerical study of drop spread and rebound on heated surfaces with consideration of high pressure.* Physics of Fluids, 2022. 34(11).

Sohag, M., W. Zhang, and X. Yang, *Three-dimensional numerical study of two drops impacting on a heated solid surface by smoothed particle hydrodynamics.* Physics of Fluids, 2023. **35**(12).

Takabatake, T., Han, D.C., Valdez, J.J., Inagaki, N., Mäll, M., Esteban, M., Shibayama, T., 2022. Three-Dimensional Physical Modeling of Tsunamis Generated by Partially Submerged Landslides. J. Geophys. Res. Ocean. 127. https://doi.org/10.1029/2021JC017826

Tarwidi, D., Redjeki, S., Adytia, D., Apri, M., 2023. MethodsX An optimized XGBoost-based machine learning method for predicting wave run-up on a sloping beach. MethodsX 10, 102119. https://doi.org/10.1016/j.mex.2023.102119

Tian, L., Lei, J., Mao, P., Xie, W., 2025. Landslide-Induced Wave Run-Up Prediction Based on Large-Scale Geotechnical Experiment : A Case Study of Wangjiashan Landslide Area of Baihetan Reservoir , China. Water.

Usama, M.M., Gardezi, H., Jalal, M.F.E., Rehman, M.M.A., Javed, M.N., Janjua, D.S., Iqbal, M.M., 2023. Predictive Modelling of Compression Strength of Waste Gp/Fa Blended Expansive Soils Using Multi-Expression Programming. Constr. Build.

https://doi.org/10.5194/egusphere-2025-4396
Preprint. Discussion started: 23 September 2025

Mater. 392, 131956. https://doi.org/10.2139/ssrn.4227552

Wang, J., Wang, S., Su, A., Xiang, W., Xiong, C., Blum, P., 2021. Simulating landslide-induced tsunamis in the Yangtze River at the Three Gorges in China. Acta Geotech. 16, 2487–2503. https://doi.org/10.1007/s11440-020-01131-3

Wang, J., Ward, S.N., Xiao, L., 2015. Numerical simulation of the december 4, 2007 landslide-generated tsunami in Chehalis Lake, Canada. Geophys. J. Int. 201, 372–376. https://doi.org/10.1093/gji/ggv026

Wang, W., Chen, G., Yin, K., Wang, Y., Zhou, S., Liu, Y., 2016. Modeling of landslide generated impulsive waves considering complex topography in reservoir area. Environ. Earth Sci. 75, 1–15. https://doi.org/10.1007/s12665-016-5252-y

Wang, Y., Liu, J., Li, D., Yan, S., 2017a. Optimization model for maximum tsunami amplitude generated by riverfront landslides based on laboratory investigations. Ocean Eng. 142, 433–440. https://doi.org/10.1016/j.oceaneng.2017.07.030

Wang, Y., Liu, J., Li, D., Yan, S., 2017b. Optimization model for maximum tsunami amplitude generated by riverfront landslides based on laboratory investigations. Ocean Eng. 142, 433–440. https://doi.org/10.1016/j.oceaneng.2017.07.030

Ward, N. Steve, Day, Simon, 2011. The 1963 Landslide and Flood at Vaiont Reservoir Italy. A tsunami ball simulation. Ital. J. Geosci. 130, 16–26. https://doi.org/10.3301/ijg.2010.21

Watts, P., 1998a. Wavemaker Curves for Tsunamis Generated by Underwater Landslides. J. Waterw. Port, Coastal, Ocean Eng. 124, 127–137. https://doi.org/10.1061/(asce)0733-950x(1998)124:3(127)

Watts, P., 1998b. Wavemaker curves for tsunamis generated by underwater landslides. J. Waterw. Port, Coast. Ocean Eng. 124, 1998.

Wiguna, E.A., 2022. Development of Real-Time Tsunami Early Warning System Dashboard Based on Tunami-F1 and Machine Learning in Sunda Arc , Indonesia, in: 2022 IEEE Ocean Engineering Technology and Innovation Conference: Management and Conservation for Sustainable and Resilient Marine and Coastal Resources (OETIC). IEEE, pp. 23–29. https://doi.org/10.1109/OETIC57156.2022.10176243

Wu, Y., Liu, L.-F.P., Hwang, K., Hwung, H.-H., 2018. A unified runup formula for breaking solitary waves on a uniform beach, in: Costal Engineering Proceedings.

Wunnemann, K., Weiss, R., 2015. The meteorite impact-induced tsunami hazard. Philos. Trans.

https://doi.org/10.5194/egusphere-2025-4396
Preprint. Discussion started: 23 September 2025

910 Yarkoni, T., Westfall, J., 2019. Choosing prediction over explanation in psychology:
911 lessons from machine learning. Prospect psychol Sci. 12, 1100–1122.
912 https://doi.org/10.1177/1745691617693393.

913 Yang, X. and S.-C. Kong, *3D Simulation of Drop Impact on Dry Surface Using SPH*
914 *Method.* International Journal of Computational Methods, 2018. 15(03): p.
915 1850011.

916 Young, A.P., Guza, R.T., Matsumoto, H., Merri, M.A., Reilly, W.C.O., Swirad, Z.M.,
917 2021. Geomorphology Three years of weekly observations of coastal cliff erosion
918 by waves and rainfall Mean Profile Change (m). Geomorphology 375.
919 https://doi.org/10.1016/j.geomorph.2020.107545

920 Zhao, T., Utili, S., Crosta, G.B., 2016. Rockslide and Impulse Wave Modelling in the
921 Vajont Reservoir by DEM-CFD Analyses. Rock Mech. Rock Eng. 49, 2437–2456.
922 https://doi.org/10.1007/s00603-015-0731-0

923